Crystal distortions and structural defects at several scales generated during the growth of silicon contaminated with carbon

H. Ouaddah, G. Regula, G Reinhart, I. Périchaud, J. Baruchel, F. Guittonneau, L. Barrallier, T.N. Tran Caliste, Nathalie Mangelinck-Noël

Crystal distortions and structural defects at several scales generated during the growth of silicon contaminated with carbon

H. Ouaddah[1], G. Regula[1], G. Reinhart[1], I. Périchaud[1], F. Guittonneau[2], L. Barrallier[2], J. Baruchel[3], T.N. Tran Caliste[3], N. Mangelinck-Noël[1]

[1]Aix Marseille Univ, Université de Toulon, CNRS, IM2NP, Marseille, France
[2]Arts et Métiers Institut de Technologie, HESAM 2, Cours des Arts et Métiers, 13617, Aix-en-Provence France
[3]ESRF-The European Synchrotron, CS40220, 38043 Grenoble CEDEX 9, France

Abstract

For all fabrication processes of the photovoltaic (PV) industry based on silicon, grain boundaries, dislocations, and impurity contamination control during solidification remains a major challenge to improve the electrical properties. In particular, carbon (C) is a major deleterious impurity for solar cells. The combination of X-ray radiography and Bragg diffraction imaging (topography) achieved *in situ* during silicon solidification allowed us to characterise the dynamics of the growth mechanisms involved in the formation of the grain structure and of defects, related to the presence of C. *Ex situ* techniques were used to characterise the grain structure and for a more precise analysis of the defects and their associated distortion fields. In the presence of C, it is shown that the resulting grain structure is constituted by a higher proportion of high-order and incoherent twin boundaries compared with the case of pure samples. Crystal distortion is characterised at the grain scale level and at a lower scale, both *in situ* and after cooling-down. The highest distortion at the grain scale corresponds to the position of the high order twin boundaries and is accentuated during cooling-down following solidification. Locally distorted regions and sub-grains are distributed all over the samples. They are observed *in situ* during the solidification from various seeds containing C (mono-crystals, industrial ribbons and multi-crystalline samples) and are retrieved after solidification. A model implying the presence of SiC precipitates at the solid-liquid interface is proposed to explain the formation during solidification of these sub-grains and of the associated local distortion.

Keywords: silicon; carbon impurity; segregation; nucleation; distortion; sub-grains; *in situ* X-ray imaging.

1 Introduction

The control of the grain boundaries, dislocations, and impurity contamination during the solidification step, remains a major challenge to improve the electrical properties [1] for all fabrication processes of photovoltaic silicon ingots. Impurities play a major role during solidification and fabrication of solar cells from silicon. On the one hand, they modify the grain nucleation and their competition during solidification [2, 3]. On the other hand, they are at the origin and/or interact with structural defects, ultimately degrading the cell conversion efficiency [4]. Impurities can be introduced into the material intentionally (doping) or unintentionally (contamination). The furnace environment and crucible are responsible for most of the light impurity contamination and in some cases for metallic impurity contamination [5, 6]. In addition, impurities can be found in the starting feedstock used for PV applications, in particular in the case of the research and fast developing industry aiming to recycle solar cells [7].

Carbon is one of the most frequent impurities in directional solidification processes. During crystal growth of silicon, oxygen or vapour can be in contact with graphite parts (crucible support) causing the formation of carbon monoxide which can be dissolved in the melted material. This is the main source of carbon contamination in conventional silicon fabrication processes (mc-Si, HP-mc Si and cast-mono). Besides, in ribbon grown on sacrificial carbon templates, the graphite

ribbon used as a support is the predominant source of C contamination [8, 9] so that silicon fabricated using this method can be considered as an extreme case of C contamination.

Light impurities can form complexes or precipitates if locally their concentration is higher than the solubility limit. The most prevalent precipitates during the growth of silicon are silicon carbide (SiC), silicon nitride (Si_3N_4) and silicon oxides (SiO_2, SiO) because of the contamination due to the crucibles, heaters and gases [10-12]. In particular, C atoms are first placed in substitutional positions in the silicon matrix if the C concentration is lower than the solubility limit of C in silicon ($4.5\ 10^{17}$ at/cm^3 [13]). In substitutional position, C is considered as electrically inactive [14] and diffuses slowly in silicon (the diffusion coefficient is about 10^{-12} cm^2/s at 1273 K). However, during solidification, impurities with a partition ratio lower than one, like carbon [2, 13], are rejected in the liquid at the level of the solid-liquid interface [13, 15, 16]. The consequence is a continuous increase of the C concentration in the liquid close to the solid-liquid interface. Thus, the solubility limit can be reached after some time of growth and when this is the case, SiC precipitates are formed. Kalejs and Chalmers [17] proposed another mechanism of C incorporation during solidification. It involves the nucleation and growth of SiC on the solid-liquid interface and occurs under conditions of hypereutectic solidification (i.e. for concentrations higher than the eutectic concentration $C_E \approx 10^{18}$ at/cm^3 [17, 18]). Within this proposed mechanism, SiC can form by epitaxial nucleation, this implying that the first layer of SiC can be coherent with the silicon crystal. After nucleation, the growth of the SiC particle is ensured by diffusion of carbon from the surrounding liquid until the interface has sufficiently moved forward to engulf the growing SiC crystal. The size of the particles is dependent on the ratio between $\Delta C/V$ where ΔC is the difference between the solute concentration in the liquid and the eutectic concentration and V is the growth rate of the solid-liquid interface.

During solidification, convection in the liquid is another main effect to be considered. The effect of convection on precipitate formation has been investigated for example by Trempa *et al.* [19]. They showed that at low growth velocity (0.5 µm/s), convection is sufficient to homogenize the concentrations of carbon and nitrogen in the liquid. Thus, the presence of convection prevents the solubility limits and eutectic concentration to be reached above or at the interface, in such a way that precipitates do not form in the ingots. At higher growth velocities (3 µm/s to 6 µm/s), the convection intensity is not sufficient to homogenize the liquid concentration and to reduce the segregation rate of carbon and nitrogen. Hence a high concentration of precipitates is observed for these growth velocities [8, 20-22].

So, the occurrence of precipitates strongly depends on the solidification process conditions, and C is generally present as both substitutional C and silicon carbide precipitates in solidified ingots [8, 17, 23, 24]. Besides, SiC in ingots can be found in different polytypes, morphology and size (from nanometres to extensions in the solidification direction up to millimetres) [10, 17, 24] although 3C-SiC is the most prevalent polytype [25].

The presence of SiC is a major burden for the photovoltaic application. First, the presence of hard SiC precipitates can have a direct mechanical effect making it more difficult to cut ingots, which is a major issue in wafer preparation at industrial scale. Furthermore, precipitation of SiC is also responsible for defects that directly degrade the electrical properties. In particular, SiC filaments induce shunts of p-n junction and therefore reduce the solar cell conversion efficiency [26, 27]. Third, during solidification, they can also be at the origin of grain nucleation acting as efficient seeds by decreasing the nucleation undercooling [2, 10, 28, 29], thus modifying the grain structure [3] and creating the conditions for the formation of new structural defects. Moreover, grain boundary grooves at the solid-liquid interface can explain part of the phenomenon of impurity segregation at the level of grain boundaries [30], which generally enhances their electrical activity [31]. Dislocations are also generated in directionally solidified crystalline Si around precipitates such as Si_3N_4 and SiC due to the lattice mismatch of the precipitates relatively to the silicon matrix and possibly to differences in the thermal expansion coefficients during cooling.

Within this context, investigations concerning the effect of C impurity during solidification have been carried out using a comprehensive and unique approach. *In situ* studies during solidification are used to understand the dynamics of formation of the impurity-related defect formation and are coupled with additional *ex situ* techniques to fully characterise the grain structure and distortion at the different relevant spatial scales on both as-grown industrial and model samples.

2 Experimental methods and investigated samples

2.1 Investigated Samples

Several representative samples are selected to study the influence of carbon on growth and defect formation. Samples named PX1 samples are solidified using conventional multi-crystalline directional solidification process. RB samples are ribbon samples produced using the RST (Ribbon on Sacrificial Template) method [9, 32, 33]. A concentration of C up to 1-5 $\times$ 10^{18} at/cm^3 is inherent to this process. In these ribbons, the presence of SiC precipitates with a large size distribution was demonstrated by different methods [8, 9].

Moreover, 2 inches (110) FZ wafers produced with the floating zone technique by SIL'TRONIX Silicon Technologies are used. Samples are shaped out from these double side mechano – chemically polished wafers. A sample in particular attracted our attention to comply with our objective to study the effect of contamination by C. Indeed, it was significantly contaminated by C only (10^{17} at/cm^3) during the preparation for *in situ* X-ray imaging; the letter "C" is added to its label (FZ-C-IS). The sample FZ-IS is a reference sample with no contamination with C. The orientation normal to both samples is <110> whereas the orientation along the solidification direction is <111> and <110> for FZ-C-IS and FZ-IS, respectively.

The main impurity concentrations (above the detection limits) for all samples described in the manuscript are given in Table 1.

	PX1-AG / PX1-IS	**RB-AG / RB-IS**	**FZ-C-IS**	**FZ-IS**
	Oxygen (at/cm^3)			
Total O [O_i]	$4.7 \times 10^{17**}$ $6 \times 10^{17*}$	5×10^{16}	$< 10^{15}$	$< 10^{15}$
	Carbon (at/cm^3)			
Total C [C_s]	$1.6 \times 10^{18**}$ $6 \times 10^{17*}$	$1\text{-}5 \times 10^{18}$	$1.5 \times 10^{17*}$	$<10^{15}$
	Copper (at/cm^3)			
Cu	$6 \times 10^{16***}$			
	Transition metals (at/cm^3)			
		10^{13} - 10^{14}		

***Table 1**: Impurity concentrations of the selected samples. AG: as-grown, IS: In situ. Method of impurity concentration measurement:* FTIR (Fourier Transform Infra-Red), ** IGA (Ion Gas Absorption), *** GDMS (Glow Discharge Mass Spectroscopy). Values given for the sample RB-AG can also be found in [8, 33].*

Some samples are directly cut from industrial ingots and are labelled "AG" for as-grown. Others are used as seed for *in situ* X-ray imaging investigation during solidification. They are labelled "IS" for *in situ*. Due to the use of boron nitride crucibles, the IS samples are contaminated

by boron. The boron concentration is evaluated by resistivity measurements after the experiments in the non-melted (10^{17} at/cm^3) seed and solidified regions (10^{17} to 10^{19} at/cm^3). Measurements of interstitial oxygen (O_i) and substitutional carbon (C_s) concentrations are performed by FTIR (Fourier Transform Infra-Red) spectroscopy at IM2NP. Other impurity concentrations are obtained from the suppliers or producing company and are based on IGA (Ion Gas Absorption) or GDMS (Glow Discharge Mass Spectroscopy) depending on the impurity.

2.2 *In situ* investigation

The directional solidification experiments are carried out in a dedicated and unique set-up of IM2NP named GaTSBI (**G**rowth at high **T**emperature observed by **S**ynchrotron **B**eam **I**maging), which is presently installed at beamline ID19 at the European Synchrotron Radiation Facility (ESRF) and allows following *in situ* and in real-time the solidification process during growth. A detailed description of the equipment, of the imaging techniques and of previously obtained results can be found elsewhere [34, 35].

2.2.1 Solidification experiments

The samples to be solidified and characterised *in situ* (IS) in the GaTSBI device are cut to dimensions 38 mm × 5.8 mm × 0.3 mm and housed inside a pyrolytic boron nitride crucible with inner dimensions: length 40 mm, width 6 mm and depth 0.3 mm. The IS samples are heated by applying the same temperature at the bottom and top resistive heaters of the furnace up to 1373 K or 1473 K. Then, an applied temperature gradient, G_{app}, is imposed between the two resistive heaters and their temperature is increased until melting. When they are initially monocrystalline, the samples are only partially melted to keep a seed crystal. After the partial melting and the stabilization of the solid-liquid interface, a cooling rate R is applied on both heaters to start solidification. Because of the imposed vertical temperature gradient, the solidification is directional in the upward direction. After solidification, the samples are cooled down until 923 K by applying cooling rates of -14 and -13 K/min on the top and bottom heaters, respectively. Below 923 K, the natural cooling-down to room temperature of the furnace and sample is no longer monitored.

Two solidification cycles are applied to both FZ-C-IS and FZ-IS samples. The cycles include the following steps: i) partial melting to keep a seed, ii) solidification from the seed with an applied temperature gradient G_{app} = 31 K/cm and a cooling rate R = -1 K/min applied on both heaters, followed by iii) a cooling-down to room temperature. A local temperature gradient of 12 K/cm for an applied temperature gradient of 31 K/cm was measured in previous work [36]. During the first cycle, *in situ* X-ray radiographs are recorded whereas during the second one, both *in situ* X-ray radiographs and topographs are recorded.

Sample	**Cooling rate R (K/min) applied on both heaters during the solidification step**	**Applied temperature gradient (K/cm) G_{app}**
FZ-C-IS	-1	31
FZ-IS	-1	31
PX1-IS	-1	20
RB-IS	-1	20

***Table 2**: Solidification parameters of the last solidification cycle for samples processed inside the GaTSBI furnace with in situ monitoring.*

Several melting and solidification cycles are applied to samples PX1-IS and RB-IS. The processing parameters applied to the samples during their last melting and solidification cycle are gathered in Table 2. The *ex situ* investigations are conducted on the samples resulting from these last cycles.

2.2.2 *In situ* X-ray imaging during crystal growth

The samples are constantly illuminated by the X-ray synchrotron white beam during the whole melting, solidification and cooling-down sequence. X-ray radiography are recorded on a CCD camera every 3 s with an exposure time of 1 s with an optics giving 5.8 μm pixel size and 12 × 12 mm^2 field of view. The obtained X-ray radiography images are direct images of the beam transmitted through the sample. The image contrast is based on the absorption of X-rays when they cross the material as explained in our previous work [35]. X-ray radiography provides images of the solid-liquid interface progress and of its morphology. The second X-ray imaging method used during the same experiments is white beam X-ray Bragg diffraction imaging (topography) [37]. For this method, diffraction patterns are regularly recorded on X-ray sensitive films (AGFA Structurix D3-SC, 17.6×12.5 cm^2) positioned at a distance of about 300 mm from the sample during solidification with an exposure time of 0.5 s. Topographs that correspond to images of the diffraction spots associated to different {hkl} diffracting crystal planes are studied. This is a powerful technique that can be used for the characterisation of defects (dislocations, twins, domain walls, inclusions, impurity precipitates) present in the crystal volume and that allows characterizing the distortion fields [35, 38-40].

2.3 *Ex situ* investigations

2.3.1 Electron Backscatter Diffraction (EBSD)

Ex situ electron backscatter diffraction (EBSD) measurements are performed after solidification and cooling-down to room temperature using a FEG-SEM JEOL JSM 7001F equipped with a HKL Nordlys camera with either a 7.0 μm or a 0.7 μm step size depending on the studied area. Inverse pole figure (IPF) orientation maps are generated with respect to the three space directions: normal to the sample surface (z), transverse direction (y) and in the growth direction for IS samples (x). The coincidence site lattice map (CSL) is reconstructed to evidence the orientation relationship between adjacent grains and the grain boundaries with a special character. EBSD is also used to determine the misorientation along a grain boundary to evaluate its coherency.

Another method based on cross-correlation of the displacement of the EBSD Kikuchi lines induced by the crystal structure distortion [41] is also applied to characterize local distortion. On the contrary to classical EBSD, only elastic deformation or stress and more precisely, residual stress are measured. The High Resolution EBSD (HREBSD) maps using CrossCourt software allows to quantify the tensorial residual stress (elastic strain) gradients inside the grains.

2.3.2 Rocking Curve Imaging (RCI)

RCI (Rocking Curve Imaging) is another imaging technique based on Bragg diffraction that has been recently further developed at BM05 at ESRF to reveal defects in crystals [42, 43]. In this method, the crystal illuminated by a monochromatic beam is rotated with a small angle ω around the Bragg angle corresponding to a family of planes [43, 44]. The originality of RCI is that images are recorded all along the rocking curve. Local diffraction curves (each one, measured on a pixel of the detector) are generated [45]. Several maps can be extracted after the analysis of the Bragg peaks corresponding to each single pixel [46]:

a- The integrated intensity map gives information on the deviation from crystalline perfection. It can be directly compared to the results obtained by X-ray topography.

b- The peak position map gives the variation of the actual Bragg angle (i.e. variations of the crystalline parameter and/or plane rotation) compared to the one in the other zones of the crystal. In particular, it can reveal the presence of sub-grains.

c- The FWHM (full width half maximum) gives quantitative information on the local distortion / deformation of the crystal.

Let us note that by definition, b) and c) mappings need a computed Gaussian fit of the rocking curves.

In section RCI, multiple slits separated (typically 0.4 mm) to avoid overlapping of diffraction images are used simultaneously so that, the images of defects are distributed as a function of their position through the depth of the sample [43, 47]. It gives the information of the position of the defects throughout the thickness of the sample in addition to the information obtained by projection RCI.

RCI characterization (in projection and section) is carried out at the beamline BM05 at the ESRF using a 20 keV monochromatic beam. The diffracted beam profile is recorded with optics giving a 0.75 µm pixel size with 1.5 × 1.5 mm^2 field of view in projection and 0.6 µm with 1.2 × 1.2 mm^2 field of view in section.

3. Results

3.1 Dynamics of solidification in the presence of C

In situ X-ray imaging is implemented during the solidification of FZ-C-IS, PX1-IS and during the solidification from 3 superimposed industrial silicon ribbons obtained by the RST method (RB-IS) to visualize the dynamics of solidification and the evolution of the defects due to the presence of C during solidification. The sample FZ-IS is also investigated in the following as a representative case of solidification from a seed issued from zone melting without C contamination.

3.1.1 Solid-liquid interface

Figure 1 shows X-ray radiographs of the solid-liquid interface in the case of FZ-IS, FZ-C-IS, PX1-IS and RB-IS samples during direction solidification inside the GaTSBI furnace (Figures 1.a-d, respectively). As can be seen on Figure 1, the solid-liquid interface is globally smooth for all samples. The solid-liquid interface observed for all samples containing C impurity (Figures 1.b-d) is comparable to the solid-liquid interface of a pure sample FZ-IS solidified with comparable conditions (Figure 1.a). Only one example of a sample solidified from a pure FZ seed is presented here. It is worth noting that it is representative of all experiments performed using this type of seeds as well as Czochralski (Cz) seeds as can be seen in previous works [35, 48].

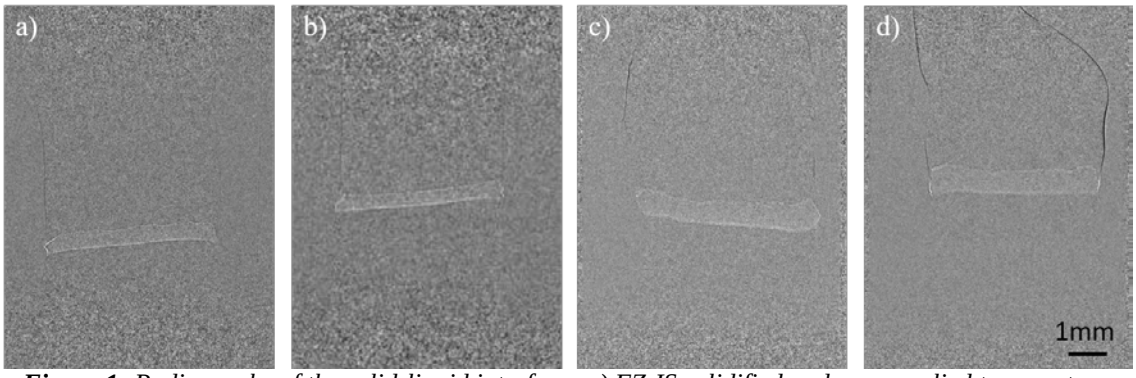

Figure 1: *Radiographs of the solid-liquid interface: a) FZ-IS solidified under an applied temperature gradient G_{app} = 31 K/cm. b) FZ-C-IS, G_{app} = 31 K/cm, c) PX1-IS, G_{app} = 20 K/cm, d) RB-IS, G_{app} = 20 K/cm. Cooling rate applied on both heaters for all samples is R = -1 K/min.*

The only particular features that are observed at the solid-liquid interface are facets at the edges and at the level of grain boundary grooves for all samples. In all cases, these facets can be characterized as {111} facets as demonstrated as well in previous works [35, 36, 40]. The presence of grain boundary grooves, which appear at the intersection between grain boundaries and the solid-liquid interface, is induced by the nucleation of several grains during directional solidification and by their competition [40].

Even for monocrystalline seeds like FZ-C-IS and FZ-IS, grain and twin nucleation take place soon after the start of solidification, so that these samples are not anymore monocrystalline. It

was shown before for FZ-IS sample and pure samples in general, that this is due to twin nucleation and subsequent competition [35, 49].

3.1.2 Grain structure, defects and distortion during directional solidification:

Figure 2.a shows the diffraction diagram of the FZ-C-IS silicon sample at the end of the solidification process. As mentioned above, this sample is <111>, <110> and <112> oriented in the solidification, normal and transverse directions, respectively.

The diffraction spots are indexed according to the Laue pattern. Topographs of the spots are obtained by observing with a microscope a single diffraction spot on the Laue diagram. Figures 2.b and 2.c correspond to $\bar{1}1\bar{1}$ and $\bar{1}1\bar{3}$ diffraction spots, respectively. Several Laue patterns similar to the one represented in Figure 2.a are recorded during solidification, which allows the dynamics of defects and distortion to be followed. Two diffraction spots, $\bar{1}1\bar{3}$ and $\bar{1}1\bar{1}$ have been selected for a more detailed analysis and for their complementarity in the characterization of defects.

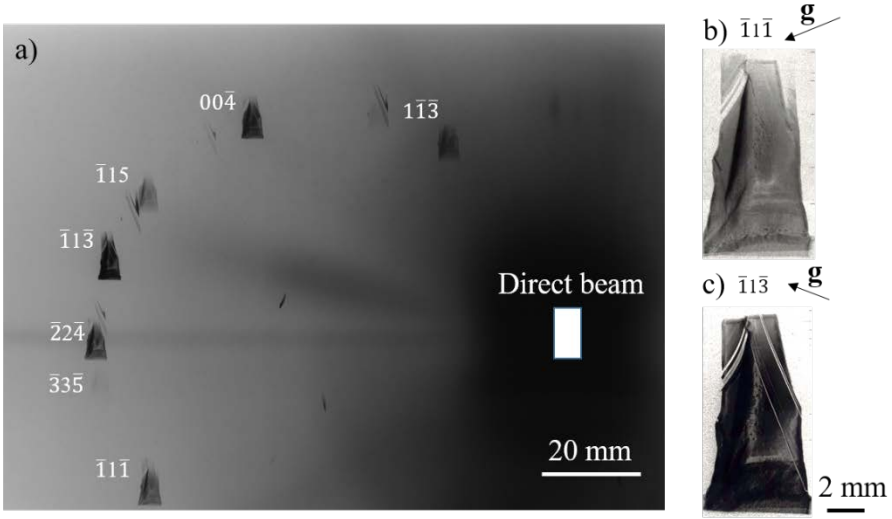

Figure 2: *a) Diffraction diagram of sample FZ-C-IS recorded at the end of the solidification (t_0 + 14 min) in the field of view (G_{app}= 31K/cm and R = -1 K/min from t_0). Enlarged topographs of b)* $\bar{1}1\bar{1}$ *and c)* $\bar{1}1\bar{3}$ *diffraction spots,* ***g*** *being the diffraction vector.*

Figure 3 shows five topographs which correspond to the $\bar{1}1\bar{1}$ (Figure 3.a-e) and $\bar{1}1\bar{3}$ (Figure 3.f-j) diffraction spot evolution during solidification. The first seed-regrown solid-liquid interface is highlighted (α in Figure 3.a) by the presence of black dots and of a darker band bounded by curves that correspond to the shape of the solid-liquid interface. During solidification, the alternation of light and dark bands is observed. For this particular experiment, the sample was partially remelted after the first solidification and the second solidification started from the position depicted in Figure 3.a. The interface is facetted and slightly tilted as highlighted by the γ label. This is also observed all along solidification (Figure 3) and by X radiography (Figure 1). Dislocations (e.g. their emergency area ε Figure 3.f-j) glide along one of the {111} family planes (their orientation is given by a blue dotted line in Figure 3). Moreover, at position highlighted by β in Figure 3.a, a black dot is observed. It is at the origin of dislocation emission as a bunch (see Figure 3.b) and contributes to the large distortion that develop (χ) during solidification. After the initial stages of solidification, twinned grains develop from the right as revealed by the straight lines on the right (Figure 3.f-j). The fact that they are only characterised on spot $\bar{1}1\bar{3}$ shows that they share the same diffraction spot $\bar{1}1\bar{1}$ with the seed [40, 50]. On the left side of the sample, twinned grains nucleate at a higher solidification height (δ in Figures 3.d and e). Pronounced distortion is observed at their level (lines that are not straight in the topograph images, δ in Figures 3.d and e). This was never observed in our previous work concerning pure monocrystalline seeds as described e.g. in Riberi-Béridot *et al.* [49]. Moreover, this distortion is accentuated during

cooling-down after solidification. Another contrast (blue arrows point to a few of them in the zoom area ϕ) that has never been characterized in samples that do not contain C impurity can be seen on the Figure 3. This contrast is particularly clear in the area (ϕ), but it is in fact present in the whole sample and in both spots. It means that homogeneously distributed local gradients of distortion are observed within the FZ-C-IS sample.

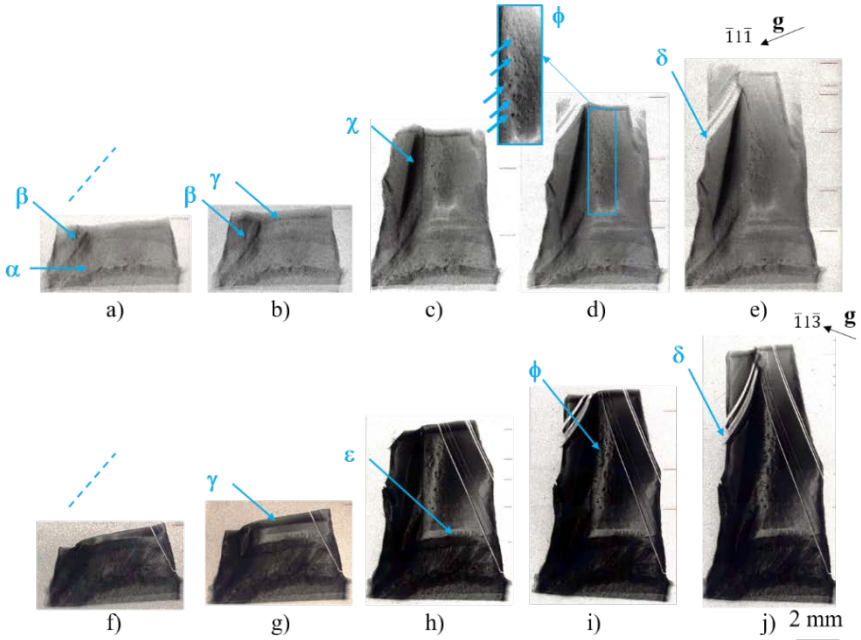

Figure 3: *FZ-C-IS: Sequence of topographs during solidification for the* $\bar{1}1\bar{1}$ *(top) and c)* $\bar{1}1\bar{3}$ *(bottom) diffraction spots. a) and f)* t_0 *: start of cooling-down at -1 K/min; b) and g)* t_0 *+ 6 min; c) and h):* t_0 *+ 9 min; d) and i):* t_0 *+ 11 min; e) and j):* t_0 *+ 14 min (end of solidification in the field of view).*

The same type of contrast is observed *in situ* during the solidification of the PX1-IS sample with a seed originating from conventional industrial directional solidification processes (Figure 4), in which a C contamination is also measured (Table 1). A few of them only are pointed out in Figure 4.a with blue arrows but they are retrieved at several places and all along solidification (Figure 4). The fact that these particular contrasts are observed *in situ* in FZ-C-IS and PX1-IS samples during growth also demonstrates that these are growth features and that they do not form during subsequent cooling-down.

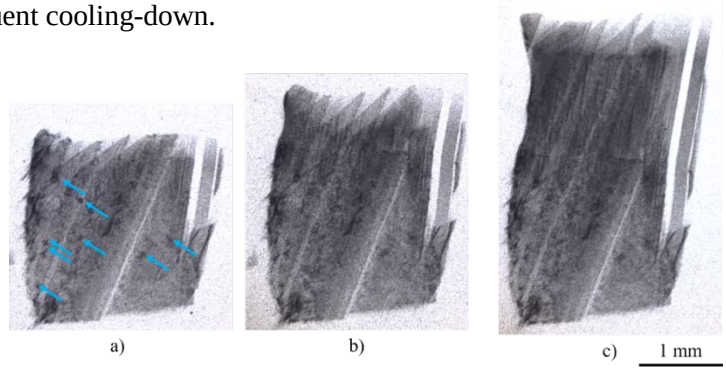

Figure 4: *Topographs for one spot during the solidification of sample PX1-IS (*G_{app} *= 20 K/cm and R = -1 K/cm applied on both heaters at* t_0*), a)* t_0*, b)* t_0 *+120 s and c)* t_f *final time of solidification in the field of view. Blue arrows point to locally distorted areas.*

3.2 Grain structure and twinning

Regular twinning is observed during solidification and is revealed by the zebra aspect of the topographs for both FZ-C-IS and PX1-IS samples (Figures 3 and 4).

Figure 5 shows the IPF maps along the growth direction and the CSL maps from EBSD measurements after the solidification of the FZ-IS sample (Figures 5.a and b, respectively) and FZ-C-IS sample (Figures 5.c and d, respectively).

After a few millimetres of solidification from the monocrystalline seed, nucleation of grains is observed in sample FZ-IS. The EBSD maps (Figure 5.a-b) confirm that these are twinned grains. In the pure sample (FZ-IS), the majority of first nucleation events is based on Σ3 twinning as seen in all previous experiments on this type of samples and as reported before [40, 49]. For first stages of solidification, only Σ3 twins are observed along the {111} facet positions for the corresponding orientation of the seed (Figures 5.a-b) and the same orientation is alternately retrieved as seen on the IPF map (Figure 5.a).

An unusual grain structure compared to pure samples hitherto investigated is observed in the FZ-C-IS sample. This is clearly seen on the IPF map (Figure 5.c) where the grain crystallographic orientation on the left hand side is not restricted to only two orientations (red, blue and purple colours on Figure 5.c) and characterised in the CSL map by higher order twin aligned along the {111} plane directions of the seed (blue and yellow boundaries in Figure 5.d).

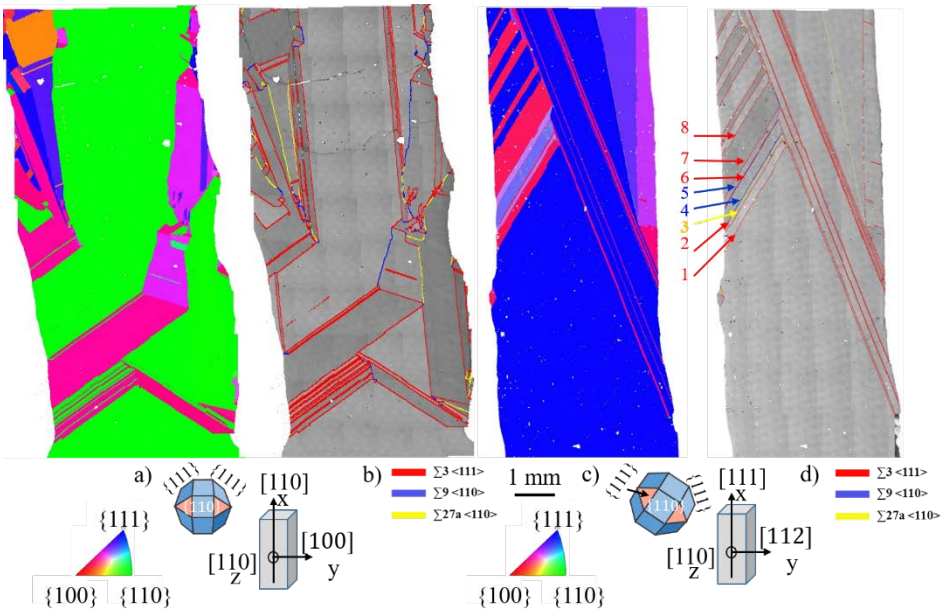

Figure 5: *Grain structure after solidification. FZ-IS sample: a) IPF map along the growth direction, b) CSL map. FZ-C-IS sample: c) IPF map along the growth direction, d) CSL map. The orientation of each sample and the corresponding position of the {111} facets are given below.*

Besides, the observation of the grain structure of FZ-C-IS after solidification (Figures 5.c-d) shows that the distortion at the level of the twin boundaries observed on the topograph (δ Figure 3) does not correspond to the shape of the twin boundaries which are in fact perfectly straight as can be seen on the EBSD maps after cooling-down to room temperature (Figures 5.c-d). Their aspect on topographs correspond to a local distortion of the crystal for which topography is very sensitive.

The grain structure of the PX1-IS sample (Figure 6) is fully multi-crystalline and more disordered compared to the FZ-C-IS and FZ-IS samples (Figure 5) although a majority of twin boundaries is also observed.

To get more detailed information regarding the crystalline quality of the grain boundaries, the pole figures obtained from the EBSD measurements are further analysed. In the pure sample, FZ-IS, (Figures 5.a and b) and also in [35, 40], the Σ3 twin boundaries are all symmetrical {111} / {111} with a misorientation ranging between 59.6 to 60 ° which denotes the high crystalline quality of these twin boundaries.

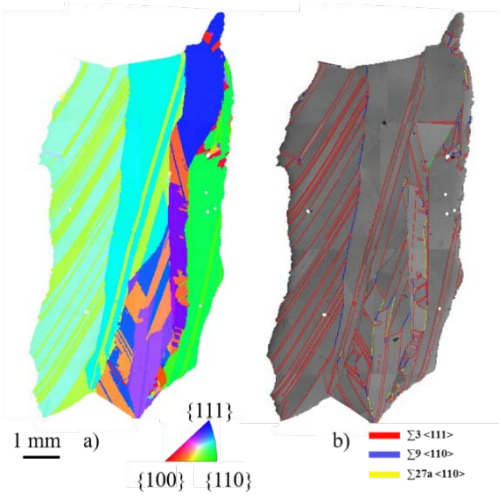

Figure 6: *Grain structure after solidification. a) IPF map along the growth direction of PX1-IS sample, b) CSL map.*

Oppositely, a very different configuration is characterised in the FZ-C-IS sample. The first twin boundary trace corresponding to a grain that nucleated on the left (1 in Figure 5.d) is a Σ3 twin symmetrical {111} / {111} with a misorientation measured between 59.69 – 59.92° along the twin boundary which shows that it is a high-quality grain boundary of the same type as the ones characterised in all experiments concerning samples grown from FZ and Cz seeds. However, the second twin boundary trace that can be characterised on the left (2 in Figures 5. d) is a Σ3 twin symmetrical {112} / {112} which is incoherent and corresponds to the second most densely packed plane at the level of the twin boundary [51]. It means that although it is a Σ3 twin boundary, it is of lower crystalline quality compared to the first twin. The third twin boundary trace (3 in Figures 5. d) corresponds to a Σ27 twin symmetrical {115} / {115}. By observing the CSL and IPF maps on Figure 5.c, it seems that the twinned grain with a Σ27 boundary nucleated close to a white dot on the CSL map. These white colour dots are non-indexed regions by the EBSD implying that they do not correspond to silicon phase, and correspond to a second phase defect. As a subsequent step, two Σ9 twinned boundaries are observed (4 & 5 in Figures 5. d). They correspond to two symmetrical {114} / {114} twin boundaries which does not correspond again to the highest crystalline quality for this type of twinned grains [51]. At last, on the top of the sample, classical Σ3 twin boundaries are observed and appear successively as in FZ and Cz samples. Again the misorientation, which is directly related to the degree of coherency, is measured to range in between 59.87 – 60° for twin boundary 7 and 59.74 – 60° for twin boundary 8.

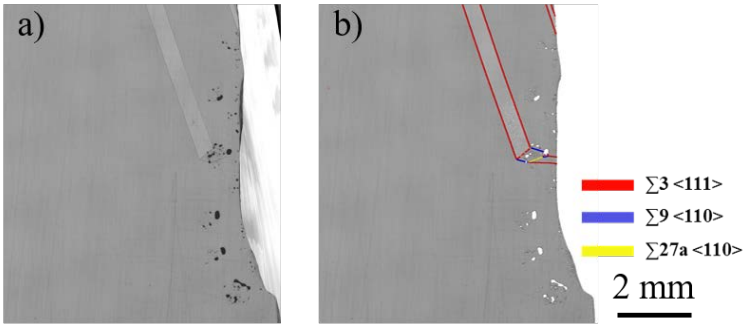

Figure 7: *Right side of FZ-C-IS at the level of the first twinning a) band contrast map, b) CSL map showing the different types of twin boundaries.*

At the scale of the sample, the behaviour on the right side of the same sample seems to be comparable with the case of pure samples (see Figures 5.b and 5.d) i.e. Σ3 twin boundaries aligned along {111} facets are observed. However, this is not the case as can be seen on the high

resolution EBSD maps which are measured at the level of the first twin that nucleated on the right (Figure 7). Figure 7 shows that Σ9 and Σ27 nucleation occur again at the level of a white dot on Figure 7.b. After this and as on the other side, the more energetically favourable configuration consisting of alternating Σ3 twin boundaries is retrieved.

3.3 Characterisation of the defects after solidification

Composition measurements confirm the presence of C in RB-AG/RB-IS, PX1-AG/PX1-IS and FZ-C-IS (Table 1).

The FZ-C-IS sample is analysed in more details because of its interest for the discussion. After a polishing step, FTIR measurement is performed on a surface delimitated by a circular mask of a few millimetres in diameter and shows that the content in C in substitutional position, C_s, is 1.5 10^{17} at/cm^3. Moreover, EDX analyses are also carried out using a Field-Emission Gun Scanning Electron Microscope (FEG-SEM) equipped with an Energy-Dispersive X-ray Spectrometer (EDX) that provides qualitative and semi-quantitative analysis of elemental C composition not limited to substitutional positions.

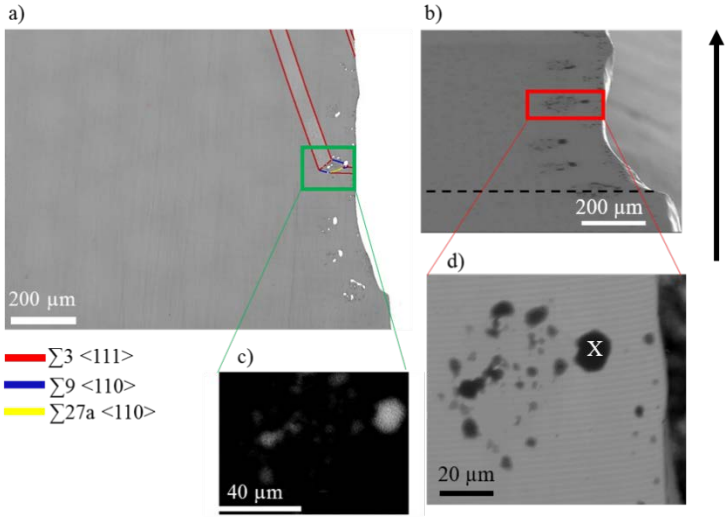

Figure 8: *a) CSL map of sample FZ-C-IS, b) SEM image, the black dotted line indicates the position of the seed-regrown interface, c) and d) BSE (Backscattered-electron) image and EDX carbon map showing different size of precipitates and their regular arrangement along the solidification direction indicated by the black arrow. The white cross points out the position of the vertical EDX scan displayed in Figure 9.*

Figure 8 shows a CSL map and a SEM image at a location close to the seed-regrown interface on the right side of FZ-C-IS also corresponding to Figure 7. The close-ups in Figures 8.c and 8.d confirm the large distribution of cluster sizes. This is confirmed by the measurements in all other regions of the sample that are investigated. The black contrast features (Figure 8.d) are distributed regularly in the solidification direction (black arrow Figure 8) showing a large range of dimensions and have never been characterised in pure FZ samples.

A representative chemical characterization of one of these black features, corresponding to the white cross in Figure 8.d, can be seen in Figure 9. To avoid superimposition of the concentration profiles of neighbour black areas, the profile was measured in the direction along the vertical (solidification) direction. The measurements performed by EDX show that these black spots are primarily constituted of C and correspond to C clusters at the surface of the sample. These regions thus appear in white (no indexation) on the EBSD IPF or CSL maps because they constitute a second phase with respect to the silicon matrix (e.g. Figure 7.b).

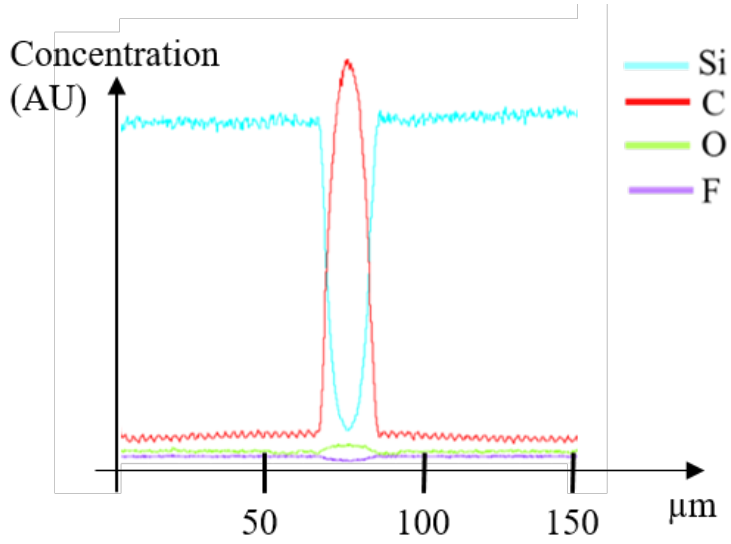

Figure 9: *EDX measurement on sample FZ-C-IS: Relative concentration profiles (C (red), Si (light blue), O (green) and F (purple)) centred on the largest black contrast feature (white cross in Figure 8.d).*

These second phase regions have been evidenced at the surface of FZ-C-IS sample but also for RB-AG samples and can be reasonably associated to the presence of C according as well to previous work on RST [8].

To obtain quantitative characterisation of the local distortion observed *in situ* on the topographs (Figures 2 & 3), RCI is performed *ex situ* on FZ-C-IS. Figure 10 shows the peak position (PP) and full-width half maximum (FWHM) maps obtained by projection RCI for the {111} diffraction spot. The RCI in projection and section are performed in the central region of the sample FZ-C-IS (see e.g central region of Figures 5.c and d) which is a region situated above the seed-regrown interface and without twinned grains.

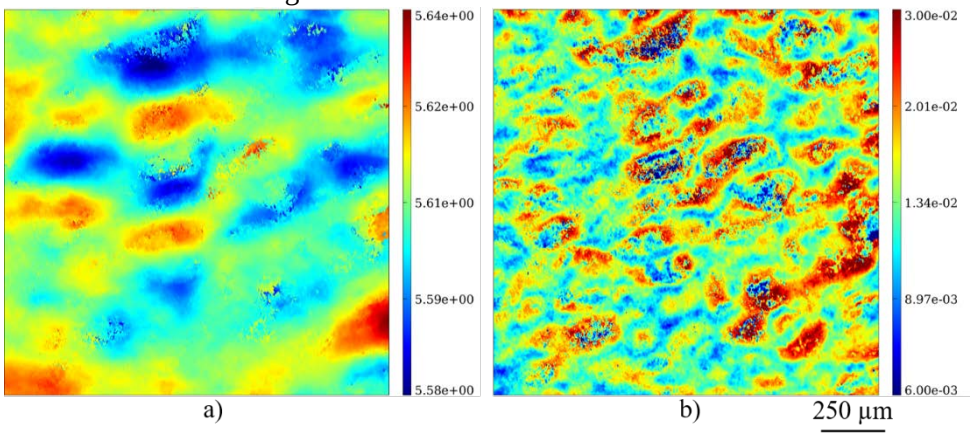

Figure 10: *FZ-C-IS sample: projection RCI ({111} diffraction spot) results with a pixel size of 0.75 µm, a field of view of 1.5 x 1.5 mm^{2}and a Bragg angle : θ_B= 5.6 °. a) Peak-Position (PP) map. The scale gives the position of the peak in degree. b) Full Width Half Maximum (FWHM) map. The scale gives the misorientation value in degree.*

The colour contrast reveals the presence of local misorientations. It also shows that these features are homogeneously distributed. As can be seen from the peak position map (Figure 10.a), the observed ellipses clearly suggest the occurrence of sub-grains displaying a range of departures from the nominal Bragg angle (5.6 °). The analysis of the rocking curve images is based on the approach described in more details in [52]. The boundaries of these sub-grains do not seem to be

abrupt, the misorientation varying gradually over 10 to 40 µm. The misorientation value is evaluated repeatedly at the level of these features between 1×10^{-2} ° to 2×10^{-2} ° in average with an uncertainty of 10 %. A large corresponding distortion is measured in the FWHM map (Figure 10.b) at the positions where there is a continuous variation of the peak position (Figure 10.a).

The images presented on Figure 10 result from an integration of the diffracted signal over the thickness of the sample. To have a more precise view of these distortions and in particular to know if they are localised only at the surface or do exist in the volume, a section rocking curve analysis is also performed. All section images are recorded simultaneously on the same area as for Figure 10 using slits as described in section 2.3.2. The corresponding PP and FWHM maps are shown in Figures 11.a and 11.b, respectively. These section images correspond to virtual slices at the level of the starting position of the solid-liquid interface. They show that the features characterised as sub-grains are present in the volume and that their boundaries are restricted to smaller volumes than what the integrated images of Figure 10 could have suggested. It corresponds to the fact that the regions where two sub-grains are present on the volume appear (Figure 11) as regions where the peak position varies slowly. Moreover, the quantitative variation of peak position measured on these section images are in agreement with those measured in projection mode.

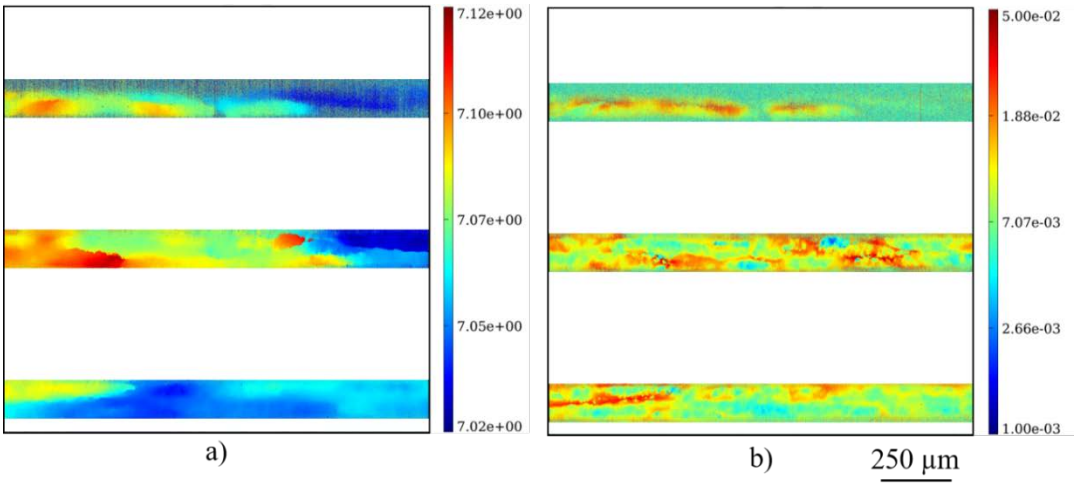

Figure 11: *FZ-C-IS sample: section RCI results ({111} diffraction spot) with a pixel size corresponding to 0.6 µm, a field of view of 1.5 x 1.5 mm² and a Bragg angle : θ_B= 7°, a) PP map. Three slits separated by 0.4 mm are used. The entrance of the X-ray beam corresponds to the bottom part of each section. The scale gives the position of the peak in degree. b) FWHM map. The scale gives the misorientation value in degree.*

Another method based on cross-correlation of the EBSD Kikuchi lines [41] is also applied on the same FZ-C-IS sample at the position where twinned grains coming from the left and right edges meet (Figures 5.c-d). Figure 12.a is a zoom of the CSL map at this position (see Figure 5.d for positioning). Figure 12.b is the representation of the Von Mises stress generally used to ease the comparison between stress tensors, and here, to represent the results as a single figure; the higher these values, the greater the elastic strain. A distortion of about 10^{-2} ° is measured at the level of the defects with this method which is consistent with the values measured using RCI at another position in the sample (Figures 10 and 11). Figure 12 shows that these local distortions are observed as well at the level of twinned grains. Complete or uncomplete elliptical shape and smaller size ones inside grains are observed highlighted by thick and thin black arrows in Figure 12, respectively. Besides, a large homogeneous distorted region (α in Figure 12) is characterised at the level of the competition region between twins coming from the right and left during solidification.

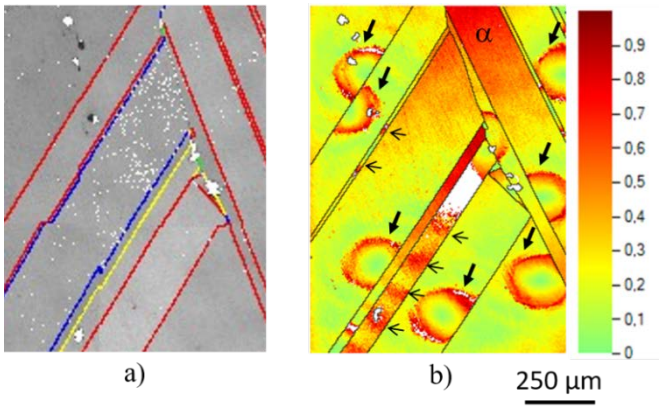

Figure 12: *FZ-C-IS: a) CSL map, b) Von Mises stress (GPa) determined by the cross-correlation method at the same position showing distorted areas with elliptical shape (thick arrows) and inside grains (thin arrows) [41].*

As shown above, the same defects are observed in FZ-C-IS and PX1-IS samples during solidification (Figures 3 and 4). They are also evidenced in Si ribbons grown on carbon sacrificial template from the industrial process. Typical EBSD maps measured on part of a silicon ribbon fabricated with the RST process of Solarforce company [8] are shown in Figure 13. For these materials, the typical grain structure is constituted of vertical grains aligned in the solidification direction bounded by Σ3 twin boundaries. This preferential orientation of the grains is due to competition under the relatively large growth rate of this process (750 µm/s) compared to more conventional directional solidification processes for which the growth rate is about 10 µm/s [53, 54].

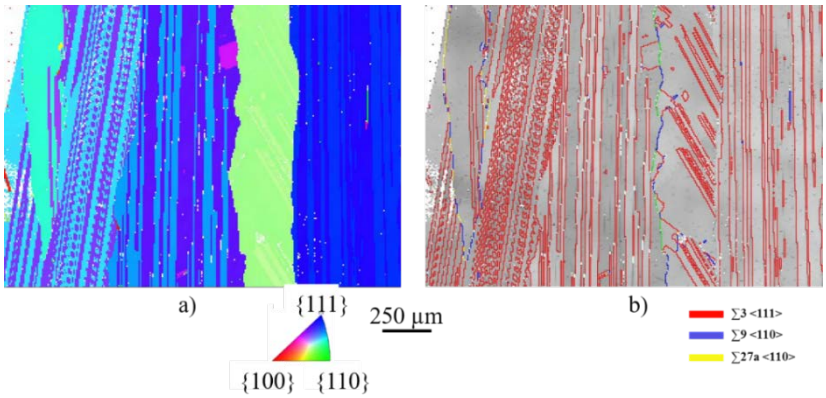

Figure 13: *Part of an industrial ribbon sample (RST-Solarforce) characterised by EBSD: a) IPF along X, b) CSL map.*

Projection RCI maps measured on RB-AG sample are presented in Figure 14. First, it shows that a larger FWHM (Figure 14.b) is measured at the level of the boundaries between the vertical Σ3 twin boundaries which also correspond to sub-grains (Figure 14.b) which is an indication of the large strain created during this process. Moreover, as for the FZ-C-IS and PX1-IS samples, defects characterized by elliptical local distortion contrast are observed (see pink arrows in Figure 14 pointing to a few of them). Again, it corresponds to sub-grains (Figure 14.a). As for the FZ-C-IS, these defects are also characterized in section RCI and therefore, they exist in the volume and not only at the surface of the samples.

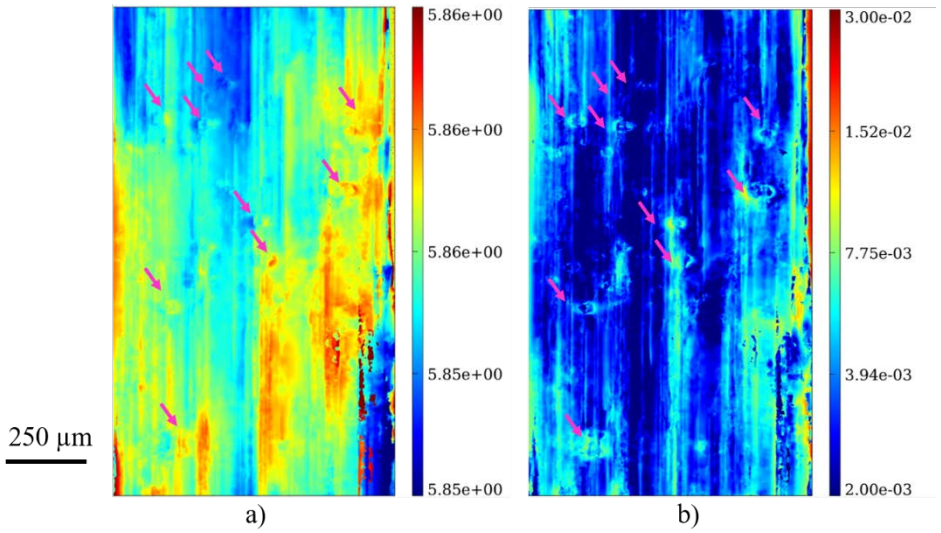

Figure 14: *RB-AG sample: projection RCI results with a pixel size of 0.75 µm. a) PP map. b) FWHM map. The scales give both quantities in degree. Pink arrows point on some of the elliptical distortion contrast.*

4. Discussion

4.1 Carbon incorporation in the crystalline structure

For the C initial concentration present in these samples, SiC precipitation during the solidification process is expected to be due to the combination of segregation during solidification and of the C solubility limit in the silicon matrix [2] or to the nucleation in hypereutectic conditions as explained in the introduction [17]. Indeed, the partition coefficient of C in silicon is lower than 1 and this implies that C segregates in the liquid close to the solid-liquid interface during solidification. When the C concentration reaches the solubility limit or the eutectic concentration, SiC particles precipitate in the liquid close to the interface or at the level of the solid-liquid interface. The almost regular distribution of large clusters along the growth direction shown in Figures 8.a and 8.b is indeed consistent with a mechanism linked to segregation during solidification and regular events of SiC precipitation. When SiC nucleation takes place, the C concentration decreases rapidly but does not come back to the initial value and the process of segregation during solidification starts again from this initial value.

The black spots and band contrast observed as well *in situ* (Figure 3) can also be related to the accumulation of C (bands) and to the formation of SiC (black dots). In fact, the variation of the contrast in the vertical direction (horizontal bands) on the topographs reveal mismatch variations during solidification due to the presence of C [55, 56] although the precise values are generally not known at temperatures close to the melting temperature. The observation of bands and of black dotted contrast aligned with the solid-liquid interface is also in agreement with the repetitive mechanism of C accumulation followed by SiC precipitation. The *in situ* characterisation, as well as the *ex situ* one demonstrates that this is a mechanism occurring during solidification and not during subsequent cooling-down.

Corresponding observations were previously done in silicon ribbons grown by the RST method. In ribbons, supersaturation of C in the liquid is also lowered by SiC precipitation in agreement with the above mechanism [8, 33]. Additionally, in this particular process, C is incorporated all along the process because of the presence of the sacrificial ribbon made of C which regularly enhances the concentration in C during pulling. This mechanism of enhancement

of the C concentration takes place on top of the C accumulation in the liquid at the solid-liquid interface due to the partition ratio.

It is worth noting that SiC particles cannot be easily directly revealed depending on their size as mentioned in the literature [17]. Besides, the engulfment of the SiC precipitates at the level of the solid-liquid interface implies complex mechanisms studied for example by Tao *et al.* [57] and in Kalejs and Chalmers [17]. The engulfment or push up of the precipitates depends on their shape and size but also on the solidification conditions. C and/or SiC precipitates can also segregate preferentially at the grain boundary grooves at the solid-liquid interface which leads to C segregation at the level of grain boundaries [30].

It is seen in Figure 1 that no destabilization of the solid-liquid interface is observed in presence of C. In fact, the above-described repetitive mechanism of SiC precipitation prevents sufficient accumulation of C at the solid-liquid interface to reach the conditions for constitutional undercooling destabilisation of the solid-liquid interface as discussed in more details in our previous work [3, 48].

4.2 Impact of C on the grain structure and grain scale distortion

A main result of previous *in situ* investigations based on pure silicon seeds is that only Σ3 type twinned grains nucleate during growth of pure (FZ seeding) or Cz seeding samples. In these pure silicon seeds, higher order twin boundaries are only created due to competition between the Σ3 type twinned grains that can meet during solidification [35, 40]. The characteristics of the grain boundaries due to competition are a consequence of the crystallographic orientations of the adjacent grains. For samples from FZ seeding only, the majority of twin boundaries are of Σ3 type (typically more than 90 %) [3]. Whereas the proportion of Σ3 twin boundaries is regularly retrieved for these pure seed samples, the proportion of higher order twin boundaries depends on the dynamics of the competition between the Σ3 twinned grains, on their relative orientation which is directly related to the seed orientation [58] and on statistical spurious grain nucleation as for example on the right side of FZ-IS (Figure 5.b). As the samples grow, more Σ3 twin grains nucleate so that grain encounters are more likely to occur increasing the amount of higher order twin boundaries as the solidification length increases.

The present results show that the grain nucleation, competition and establishment of the grain structure are affected by the presence of SiC and C so that the mechanism described just above does not apply to all nucleation events during growth of the FZ-C-IS sample. The comparison between the *in situ* experiments (Figures 1.b, 2 and 3) and the *ex situ* EBSD maps (Figures 5.c-d) shows that the twin grains corresponding to the Σ27 and Σ9 twin boundaries on the left hand side of the FZ-C-IS sample nucleated during solidification along {111} facets. The fact that a white/black contrast is observed by EBSD close to some location of nucleation of the higher order twins on the left (Figures 5.c-d) and more locally on the right-hand side (Figures 7 and 8) of sample FZ-C-IS is in favour of a nucleation mechanism enhanced by carbon and associated to SiC precipitates or to the presence of C. It is worth mentioning that this is the only situation for which a twin nucleation different from Σ3 is observed during our *in situ* experiments up to now.

It was proven with electromagnetic levitation studies by Beaudhuin *et al.* [10] that the presence of SiC precipitates reduces the nucleation undercooling of the first Si crystals. As a consequence, the undercooling needed for a new grain nucleation (nucleation undercooling) is lowered on precipitates so that nucleation can take place for lower growth undercoolings in the presence of SiC precipitates at the level of the solid-liquid interface which can explain the observation of unusual grain nucleation in the presence of C in FZ-C-IS. Finally, there is a higher probability of Si grain nucleation in the presence of SiC which affects directly the grain structure by increasing the number of grains. This mechanism was invoked to explain the so called “grits” formation in the mc-Si industrial processes in the model from Mangelinck-Noël *et al.* [59]. This model was later revisited by Beaudhuin et *al.*[2]. However, not all precipitates are at the origin of new grains. Indeed, if this was the case, much more grain nucleation would be observed as it can be seen for example in Figure 7.

In previous work, the grain boundary types in samples containing different impurities were characterised and showed that higher order twins and random angle grains nucleate when C and O are present [3]. The impact of a high concentration of C inherent to the process has also been studied in Si ribbons grown on carbon sacrificial template. Again, the consequence of the presence of a high C concentration was the formation of SiC precipitates which affected the grain structure and defects [5].

At a finer level, non-symmetrical or incoherent twin boundaries are observed in the FZ-C-IS sample as described in section 3.2. Several twin boundaries do not correspond to the most energetically favourable configuration (symmetric and coherent): Σ3 twin boundary symmetrical {112} / {112} (2 in Figures 5.c and d), Σ27 twin boundary symmetrical {115} / {115} (3 in Figures 5.c and d) and two Σ9 twin boundaries {114} / {114} which do not correspond to the highest crystalline quality for this type of twinned grains as well (4 & 5 in Figures 5.c and d) [51]. However, it is striking that they all align along the {111} facets even if it implies that their configuration does not correspond to the highest crystalline quality. This can be related to their nucleation at the level of {111} facets which can be enhanced by the presence of carbon and SiC [60]. Although the nucleation mechanism would need to be further investigated, this is the signature of the presence of defects in general and in particular of distortions and dislocations at the level of the twin boundaries. Even the usual Σ3 alternation that finally takes over shows a higher degree of incoherency than usually observed in pure samples (deviation of the angle from 60° and unsymmetrical configuration) which is the signature of dislocations inside the twin boundaries. The lower crystalline quality is also evidenced by the global distortion of the crystal structure observed on the topographs at the location of these particular twin boundaries during solidification (Figures 2.c and 3.j) and after cooling-down.

The lower crystalline quality of the twin boundaries is of critical importance as it was shown that this has a direct impact on electrical and photovoltaic properties [4, 61]. Such incoherent or high order twin boundaries are prone to impurity segregation and to dislocation emission that further degrade the electrical properties [62].

4.3 Defects, local distortion and mechanism of sub-grain formation

Dislocations

When increasing the temperature, dislocations nucleate from the sample edges or from the melting interface used to prepare the seed. Dislocation propagation occurs throughout the entire width or length of the seed with the activation of specific crystallographic slip planes depending on the seed crystallographic orientation and on the forces applied due to the crucible-sample configuration [63]. Dislocations are observed in the seed region and lay in a particular family of {111} glide planes. On FZ-C-IS, it results in diagonal activated slip systems seen inside the seed (Figure 3). During solidification from the initial seed, part of the dislocations initially in the seed is not transmitted at the regrown interface, as can be seen on ε Figure 3. In fact, dislocations can glide at the level of the {111} facet at the interface and exit the sample as also shown more generally in FZ samples [34]. Black contrast is observed along some of the gliding planes (Figure 3). It corresponds to the distortion induced by the presence of dislocations.

The influence of the presence of C can be seen clearly when a dislocation bunch develops from a black dot that can be related to a SiC particle according to the above discussions (see β in Figure 3.a and subsequent images in Figure 3). During solidification, SiC particles can be at the origin of dislocation emission due to the lattice mismatch compared to the silicon matrix. Let us compare the Si and SiC lattice parameters, considering 3C-SiC which is the most common polytype for SiC, the ratio between the Si matrix lattice parameter and the 3C-SiC is approximately of 1.24 from ambient to 1000 K although both lattice parameters vary with the temperature [64, 65]. However, it is worth mentioning that even a small lattice difference can create a non-negligible local strain field. Additionally, dislocations or distortion are emitted from lower crystalline quality grain boundaries that nucleate in the presence of C as seen in Figure 3 and as also inferred in experimental and modelling studies [40, 49, 51, 66, 67].

Local distortion

As mentioned above, the elliptical contrasts observed *in situ* during solidification (Figures 3, 4) and *ex situ* (Figures 10, 11, 12 & 14) demonstrate that they are growth features and that they do not form during subsequent cooling-down. These features characterized *ex situ* by RCI (Figures 10 & 11) and by the cross-correlation method (Figure 12) for FZ-C-IS and by RCI for RB-AG (Figure 14) can be directly correlated (size and distribution) to the local distortion contrast characterized *in situ* on topographs Figures 3 (ϕ) and 4 for FZ-C-IS and PX1-IS, respectively. This distortion which is associated to the presence of sub-grains is thus present during growth and is kept during subsequent cooling-down as RCI is performed *ex situ* after solidification. Moreover, the section RCI maps for both samples FZ-C-IS (Figure 11) and RB-IS (not shown) prove that these features are also observed within the thickness of the sample. All results related to these features are thus remarkably reproducible. Moreover, a noticeable quantitative agreement is obtained between the RCI and cross-correlation measurements.

In the following, a mechanism that can explain the contrast observed with RCI *ex situ* and *in situ* during solidification is stepped forward, after having explored different possible scenarios.

Crystalline defects such as precipitates, dislocations and impurities, act on the diffraction process through their associated effective misorientation angle variation $\delta\theta_m(\vec{r})$, which can be approximated by the following equation [68]:

$$\delta\theta_m(\vec{r}) = \frac{\delta d}{d}(\vec{r})tan\theta_B \pm \delta\theta(\vec{r}) \qquad (1)$$

where θ_B is the Bragg angle, $\frac{\delta d}{d}(\vec{r})$ is the local relative change of the lattice parameter and $\delta\theta(\vec{r})$, the local change in crystallographic orientation. This effective misorientation corresponds to the strain field generated by the defect [38, 68, 69]. Regions displaying a gradient of effective misorientation give rise to a "direct image" leading, in the X-ray low absorption case we are concerned with, to supplementary diffracted intensity associated to distorted regions.

The first hypothesis explored is that the observed distortion can be associated to a distortion of the crystalline structure due to the presence of C in substitutional position. Let us calculate the value that would be obtained for the distortion of the crystal structure due to the presence of C in substitutional position inside the silicon crystal. In this case, the second term of equation 1 is neglected. The literature [56] provides the following equation that relates the concentration in C within the silicon matrix and the change of the lattice parameter:

$$\Delta d/d = -6.5 \times 10^{-24} n \qquad (2)$$

where n is the C concentration in atoms/cm^3.

The Bragg angle (7.074 °) used during the RCI measurements in section is applied in equation (1) as it is a case without superimpositions on the contrary to projection RCI. For a C concentration equals to the one measured by FTIR i.e., 1.5×10^{17} at/cm^3 in sample FZ-C-IS, the value obtained for $\delta\theta_m$ using equation (1) is $\approx 7 \times 10^{-6}$ °. This value is several orders of magnitude smaller than the misorientation measured with the RCI and with the cross-correlation method (10^{-2} °). Even in the extreme cases of the PX1-IS, RB-AG and RB-IS, $\delta\theta_m \approx 7 \times 10^{-5}$ ° at maximum which is still several orders of magnitude smaller than the measured misorientation. As a conclusion, the presence of substitutional C cannot be the only mechanism invoked to explain the distortion contrast observed during solidification *in situ* and *ex situ* after solidification by both RCI and cross-correlation methods. Besides, the particular strain field due to a single precipitate would correspond to a misorientation of the order of 10^{-3} ° whereas in our case, we measure misorientations of about 10^{-2}° so that the contrast due to a single precipitate cannot be distinguished.

Moreover, the contrast observed with the peak position maps indicates that sub-grains are present and thus that the second term of equation 1 must be taken into account. A mechanism presented in the following and related to the presence of SiC during the dynamics of solidification is proposed to explain the appearance of these local distortions leading to the formation of sub-grains. The mechanism principle is illustrated in Figure 15.

As seen above, the carbon contamination causes the formation of SiC precipitates. They can be close to the solid liquid interface due to their regular precipitation or even nucleate at the solid-liquid interface [17]. It is worth noting that in the SiC nucleation mechanism proposed by Kalejs and Chalmers [17], the dependence of the maximum radius of the SiC particles on the ratio between $\Delta C/V$ where ΔC is the difference between the solute concentration in the liquid and the eutectic concentration and V is the growth rate of the solid-liquid interface is a main feature. As a consequence, they show that comparable SiC particle sizes can be found in both EFG (Edge Film-defined Film-Fed Growth) that have a higher growth rate and contamination level and FZ and CZ samples. It might be one of the reasons why the results in all our samples are comparable although they are grown in different conditions.

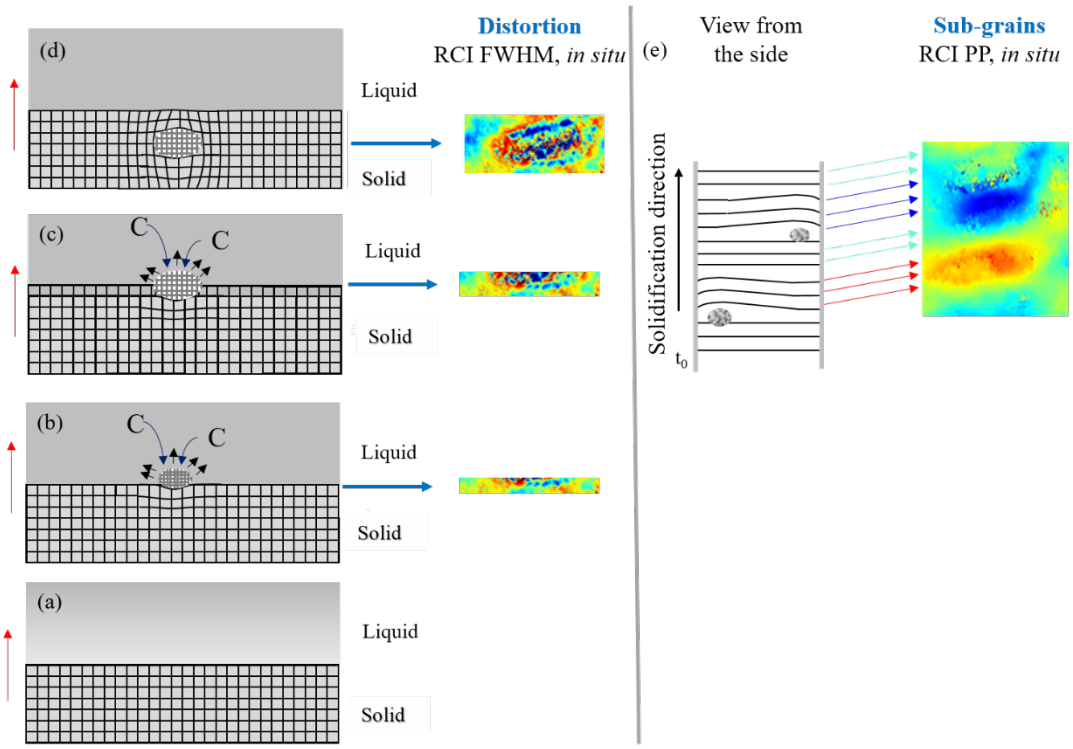

Figure 15: *Schematic illustration of the mechanism of the sub-grain formation mechanism and distortions during solidification due to the presence of SiC precipitates. a) Solid-liquid interface, b) Nucleation of a SiC precipitate, c) Competitive growth of the SiC particle and Si solid-liquid interface, d) Engulfment of the SiC precipitate, e) View from the side to explain the formation of the sub-grains during solidification. Corresponding extracts of RCI FWHM and PP maps are displayed.*

Dislocation densities up to few 10^{8} cm^{-2} can be generated due to the presence of such precipitates [70, 71]. However, the presence of dislocations is not necessary to explain the presence of sub-grains in our experiments. A smooth transition from distorted SiC crystallographic planes towards silicon crystalline structure is also possible [17].

The precipitates can grow due to C diffusion while the solid-liquid interface continues its progress (Figure 15.b). At the level of the precipitates, the interface is slightly in advance compared to the adjacent solid-liquid interface (Figure 15.c). Consequently, the silicon growth in the neighbourhood of the precipitates is misoriented compared to the silicon solid-liquid interface growing from the seed. It is worth noting that these distorted areas do not correspond to the scale

of the precipitates but to the distortion field created by the presence of the precipitates which has a larger spatial extension. When both regions meet, a continuous sub-grain is formed to bridge the orientation at the level of the precipitates and the one of the smooth silicon solid-liquid interface from the seed (Figure 15.d) which is consistent with RCI and cross-correlation observations. The same process takes place at several locations at the solid-liquid interface as can be seen in the section RCI (Figure 11) that can be understood as a virtual slice at the solid-liquid interface bonded by a {111} facet due to the crystallographic orientation of the FZ-C-IS sample along the solidification direction. As several precipitates exist all along solidification and within the thickness, there is a competition between the areas growing on top of the precipitates (Figure 15.e) that can explain the alternation of red and blue regions in the RCI projection (Figure 10).

The cross-correlation analysis (Figure 12) corresponds to a region with twin boundaries and it shows that the twin boundaries are not affected by the elliptical sub-grains. Additionally, it also shows that the highest distortion and occurrence of sub-grains is related to the presence of the Σ9 and Σ27 twinned grains (thin arrows in Figure 12.b). The later could be due to another source of distortion e.g. smaller precipitates or to the elliptical distorted areas truncated by the twin boundaries. At last, the sub-grains formed during growth have a different morphology in this region (thick arrows in Figure 12.b) as complete elliptical shapes are not always entirely developed but seems to be cut at the level of the twin boundaries. This could be related to a favoured nucleation of the SiC nucleus at the level of the solid-liquid interface which is bounded by {111} facets at the edges of the sample (Figures 1 & 3).

The same mechanism can be extended to the case of multi-crystalline samples (PX1-IS) and ribbon samples from the industrial process (RB-AG and IS) due to the remarkable consistency of the results.

5. Conclusion and prospects

The effect of C impurity contamination on the formation of grains and structural defects during solidification for both model and industrial samples are studied. The combination of X-ray radiography and topography achieved *in situ* during the solidification of Si confirms its efficiency to unveil crystal growth mechanisms. Indeed, it successfully allows to observe the growth mechanisms involved in the formation of the grain structure and of defects that influence the material properties for photovoltaic applications. The *ex situ* techniques complement the understanding of the involved mechanisms.

In a Si samples contaminated with C, melt composition in C near the solid-liquid interface continuously increases during solidification by the segregation phenomenon due to the partition ratio of C in Si. As soon as the solubility limit or eutectic concentration is reached SiC precipitates are formed.

We show that the grain structure resulting from solidification is constituted by a higher proportion of high-order twin and of random angle grain boundaries for C-contaminated samples compared with the case of pure samples. There is a higher probability of grain nucleation enhanced by the presence of C not all related to the energetically Σ3 twin most favourable nucleation in pure samples. Moreover, even Σ3 twin boundaries show a higher level of incoherency in comparison to pure samples so that they are more prone to impurity segregation.

Additionally, in the presence of C, the distortion of the crystal structure is characterised at several scales: grain scale and locally both *in situ* and after cooling-down. Distortion at the grain scale appears during solidification where higher order twin boundaries are formed and is accentuated during solidification and subsequent cooling-down. Bunches of dislocations can also be directly related to the presence of SiC precipitates. Moreover, as revealed by *in situ* and *ex situ* X-ray diffraction imaging, local distortion regions of the crystalline structure corresponding to sub-grains are distributed all over the samples. They are observed during solidification from seeds of different types of samples containing C (mono-crystal, industrial ribbons and multi-crystalline sample) and are retrieved after solidification. We propose a mechanism in which these features are formed during solidification in the presence of SiC precipitates. The growing silicon just

above the precipitates is misoriented compared to the solid-liquid interface of silicon growing from the seed. When both regions meet, sub-grains result and compete with each other due to the presence of precipitates all over in the sample volume.

These results show the main impact on the formation of the grain structure and defects at different scales of the presence of C while growing silicon. These growth features that remain after solidification have a severe impact on electrical and further on photovoltaic properties of the material.

Acknowledgments

The work has been partly supported by the ANR Project CrySaLID (Nº ANR-14-CE05-0046-01). The ESRF (European Synchrotron Radiation Facility) BM05 and ID19 teams are greatly acknowledged for support during the *in situ* X-ray and *ex situ* Rocking Curve Imaging experiments. The Solarforce team is acknowledged to have provided ribbon parts.

References

[1] G. Stokkan, Y. Hu, Ø. Mjøs, M. Juel, Study of evolution of dislocation clusters in high performance multicrystalline silicon, Sol Energ Mat Sol C 130 (2014) 679-685.

[2] M. Beaudhuin, T. Duffar, M. Lemiti, K. Zaidat, One-dimensional model of the equiaxed grain formation in multi-crystalline silicon, Journal of Crystal Growth 319(1) (2011) 106-113.

[3] H. Ouaddah, I. Périchaud, D. Barakel, O. Palais, M. Di Sabatino, G. Reinhart, G. Regula, N. Mangelinck-Noël, Role of Impurities in Silicon Solidification and Electrical Properties Studied by Complementary In Situ and Ex Situ Methods, physica status solidi (a) 1900298 (2019) 1-10.

[4] K. Adamczyk, R. Søndenå, G. Stokkan, E. Looney, M. Jensen, B. Lai, M. Rinio, M.D. Sabatino, Recombination activity of grain boundaries in high-performance multicrystalline Si during solar cell processing, Journal of applied physics 123(5) (2018) 055705.

[5] C. Kranert, M. Trempa, C. Reimann, J. Friedrich, Metal contamination of silicon from the furnace atmosphere after crystallization, Journal of Crystal Growth 559 (2021) 126026.

[6] C. Reimann, M. Trempa, T. Jung, J. Friedrich, G. Müller, Modeling of incorporation of O, N, C and formation of related precipitates during directional solidification of silicon under consideration of variable processing parameters, Journal of Crystal Growth 312(7) (2010) 878-885.

[7] L. He, S. Yuan, Y. Xu, Q. Lei, W. Mao, H. Luo, X. He, X. Li, L. Wang, D. Yang, Y. Qian, Evaluation of large-scale recycled seed for cast monocrystalline silicon: Defect multiplication mechanisms and feasibility, Sol Energ Mat Sol C 230 (2021) 111266.

[8] B. Heilbronn, F. De Moro, E. Jolivet, E. Tupin, B. Chau, R. Varrot, B. Drevet, S. Bailly, D. Rey, H. Lignier, Y. Xi, T. Riberi-Béridot, N. Mangelinck-Noël, G. Reinhart,

G. Regula, Fast growth of thin multi-crystalline silicon ribbons by the RST method, Crystal Research and Technology (2014) 1-14.

[9] C. Belouet, M. Monville, C. Bigot, E. Jolivet, R. Varrot, J. Chancolon, S. Bonnamy, The carbon substrate in RST Si ribbon technology for solar cells, Carbon 141 (2019) 427-443.

[10] M. Beaudhuin, G. Chichignoud, P. Bertho, T. Duffar, M. Lemiti, K. Zaïdat, Carbon reaction with levitated silicon-Experimental and thermodynamic approaches, Materials Chemistry & Physics 133 (2012) 284-288.

[11] E. Undheim, K.E. Ekstrøm, L. Arnberg, R. Holmestad, M. Di Sabatino, The effect of holding time on the size distribution of β-Si3N4 particles and nucleation undercooling in multicrystalline silicon, Physica Status Solidi c 13(10-12) (2016) 822-826.

[12] E. Undheim, P.E. Vullum, R. Holmestad, L. Arnberg, M. Di Sabatino, Orientation relationship between β-Si3N4 and Si in multicrystalline silicon ingots for PV applications, Journal of Crystal Growth 495 (2018) 14-19.

[13] F. Durand, J.C. Duby, Carbon solubility in solid and liquid Silicon-A review with reference to eutectic equilibrium, Journal of Phase Equilibria 20(1) (1999) 61-63.

[14] O. Palais, Cartographie de durées de vie des porteurs minoritaires et d'impuretés métalliques dans le silicium cristallin par déphasage micro-ondes Thèse de l'Université Paul Cézanne, Marseille, France, 2000.

[15] W. Kurz, D.J. Fisher, Fundamentals of solidification, Trans Tech Publications, Aedermannsdorf-Switzerland, 1986.

[16] F. Durand, J.C. Duby, Solid-liquid equilibria in the silicon-rich corner of the Si-O-C system, Journal of Phase Equilibria 21(2) (2000) 130-135.

[17] J.P. Kalejs, B. Chalmers, Melt-interface mechanism for generation of silicon carbide microdefects in silicon, Journal of Crystal Growth 79(1) (1986) 487-492.

[18] T. Nozaki, Y. Yatsurugi, N. Akiyama, Concentration and Behavior of Carbon in Semiconductor Silicon, J Electrochem Soc 117(12) (1970) 1566.

[19] M. Trempa, C. Reimann, J. Friedrich, G. Müller, The influence of growth rate on the formation and avoidance of C and N related precipitates during directional solidification of multi crystalline silicon, Journal of Crystal Growth 312(9) (2010) 1517-1524.

[20] K. Arafune, T. Sasaki, F. Wakabayashi, Y. Terada, Y. Ohshita, M. Yamaguchi, Study on defects and impurities in cast-grown polycrystalline silicon substrates for solar cells, Physica B: Condensed Matter 376-377 (2006) 236-239.

[21] M.P. Bellmann, E.A. Meese, L. Arnberg, Impurity segregation in directional solidified multi-crystalline silicon, Journal of Crystal Growth 312(21) (2010) 3091-3095.

[22] S. Binetti, J. Libal, M. Acciarri, M. Di Sabatino, H. Nordmark, E.J. Øvrelid, J.C. Walmsley, R. Holmestad, Study of defects and impurities in multicrystalline silicon grown from metallurgical silicon feedstock, Materials Science and Engineering: B 159–160(0) (2009) 274-277.

[23] A.R. Bean, R.C. Newman, The solubility of carbon in pulled silicon crystals, J Phys Chem Solids 32(6) (1971) 1211-1219.

[24] H.J. Möller, L. Long, M. Werner, D. Yang, Oxygen and Carbon Precipitation in Multicrystalline Solar Silicon, physica status solidi (a) 171(1) (1999) 175-189.

[25] A. Lotnyk, J. Bauer, O. Breitenstein, H. Blumtritt, A TEM study of SiC particles and filaments precipitated in multicrystalline Si for solar cells, Sol Energ Mat Sol C 92(10) (2008) 1236-1240.

[26] O. Breitenstein, J.P. Rakotoniaina, M.H. Al Rifai, M. Werner, Shunt types in crystalline silicon solar cells, Progress in Photovoltaics: Research and Applications 12(7) (2004) 529-538.

[27] J. Bauer, O. Breitenstein, J.-P. Rakotoniaina, Electronic activity of SiC precipitates in multicrystalline solar silicon, physica status solidi (a) 204(7) (2007) 2190-2195.

[28] M.G. Tsoutsouva, T. Duffar, D. Chaussende, M. Kamguem, Undercooling measurement and nucleation study of silicon droplets on various substrates, Journal of Crystal Growth 451 (2016) 103-112.

[29] L. Sylla, A. Hodroj, N. Mangelinck-Noël, T. Duffar, Measurement of undercooling for better understanding of solidification phenomena during the elaboration of polycrystalline silicon, 19th European Photovoltaic Solar Energy Conference and Exhibition, Paris, France, 2004, p. 3775.

[30] K. Fujiwara, M. Ishii, K. Maeda, H. Koizumi, J. Nozawa, S. Uda, The effect of grain boundary characteristics on the morphology of the crystal/melt interface of multicrystalline silicon, Scripta Materialia 69(3) (2013) 266-269.

[31] A. Lamzatouar, O. Palais, O.B.M.H. Duparc, J. Thibault, A. Charaï, Relationship between structure, segregation and electrical activity in grain boundaries, Journal of Materials Science 40(12) (2005) 3163-3167.

[32] C. Bigot, C. Baillis, E. Jolivet, C. M., R. Varrot, C. Belouet, Growth of polycrystalline ribbon by the RST process; computational analysis of the mechanical stability of the cooling ribbon, CSSC-6, 2013.

[33] F. De Moro, A. Focsa, K. Derbouz, A. Slaoui, N. Auriac, H. Lignier, P. Keller, Multicrystalline silicon solar cells from RST ribbon process, physica status solidi c 9(10-11) (2012) 2092-2096.

[34] M. Becker, G. Regula, G. Reinhart, E. Boller, J.-P. Valade, A. Rack, P. Tafforeau, N. Mangelinck-Noel, Simultaneous X-ray radiography and diffraction topography

imaging applied to silicon for defect analysis during melting and crystallization, Journal of Applied Crystallography 52(6) (2019) 1312-1320.

[35] H. Ouaddah, M. Becker, T. Riberi – Béridot, M.G. Tsoutsouva, V. Stamelou, G. Regula, G. Reinhart, I. Périchaud, F. Guittonneau, L. Barrallier, J.-P. Valade, A. Rack, E. Boller, J. Baruchel, N. Mangelinck-Noël, X-ray Based in Situ Investigation of Silicon Growth Mechanism Dynamics—Application to Grain and Defect Formation, Crystals 10 (2020) 555.

[36] V. Stamelou, M.G. Tsoutsouva, T. Riberi-Béridot, G. Reinhart, G. Regula, J. Baruchel, N. Mangelinck-Noël, {111} facet growth laws and grain competition during silicon crystallization, Journal of Crystal Growth 479 (2017) 1-8.

[37] A.R. Lang, The early days of high-resolution X-ray topography, Journal of Physics D: Applied Physics 26(4A) (1993) A1-A8.

[38] R.C. Burns, A.I. Chumakov, S.H. Connell, D. Dube, H.P. Godfried, J.O. Hansen, J. Härtwig, J. Hoszowska, F. Masiello, L. Mkhonza, M. Rebak, A. Rommevaux, R. Setshedi, P.V. Vaerenbergh, HPHT growth and x-ray characterization of high-quality type IIa diamond, Journal of Physics: Condensed Matter 21(36) (2009) 364224.

[39] D. Oriwol, E.R. Carl, A.N. Danilewsky, L. Sylla, W. Seifert, M. Kittler, H.S. Leipner, Small-angle subgrain boundaries emanating from dislocation pile-ups in multicrystalline silicon studied with synchrotron white-beam X-ray topography, Acta Materialia 61(18) (2013) 6903-6910.

[40] M.G. Tsoutsouva, T. Riberi – Béridot, G. Regula, G. Reinhart, J. Baruchel, F. Guittonneau, L. Barrallier, N. Mangelinck-Noël, In situ investigation of the structural defect generation and evolution during the directional solidification of <110> seeded growth Si, Acta Materialia 115 (2016) 210-223.

[41] S.D. Salehi, M.A. Rastak, M.M. Shokrieh, L. Barrallier, R. Kubler, Full-Field Measurement of Residual Stresses in Composite Materials Using the Incremental Slitting and Digital Image Correlation Techniques, Experimental Mechanics 60(9) (2020) 1239-1250.

[42] J. Baruchel, M. Di Michiel, T. Lafford, P. Lhuissier, J. Meyssonnier, H. Nguyen-Thi, A. Philip, P. Pernot, L. Salvo, M. Scheel, Synchrotron X-ray imaging for crystal growth studies, Comptes Rendus Physique 14(2) (2013) 208-220.

[43] T.A. Lafford, J. Villanova, N. Plassat, S. Dubois, D. Camel, Synchrotron X-ray imaging applied to solar photovoltaic silicon, Journal of Physics: Conference Series 425(19) (2013) 192019.

[44] M.G. Tsoutsouva, V.A. Oliveira, D. Camel, J. Baruchel, B. Marie, T.A. Lafford, Mono-like silicon ingots grown on low angle misoriented seeds: Defect characterization by synchrotron X-ray diffraction imaging, Acta Materialia 88(0) (2015) 112-120.

[45] M.G. Tsoutsouva, V.A. Oliveira, D. Camel, T.N. Tran Thi, J. Baruchel, B. Marie, T.A. Lafford, Segregation, precipitation and dislocation generation between seeds in directionally solidified mono-like silicon for photovoltaic applications, Journal of Crystal Growth 401(0) (2014) 397-403.

[46] M.G. Tsoutsouva, V.A. Oliveira, J. Baruchel, D. Camel, B. Marie, T.A. Lafford, Characterization of defects in mono-like silicon for photovoltaic applications using X-ray Bragg diffraction imaging, Journal of Applied Crystallography 48(3) (2015) 645-654.

[47] R.T. Kluender, A. Philip, J. Meyssonnier, J. Baruchel, Three-dimensional distortion measurements by section rocking curve imaging: Application to ice crystals, physica status solidi (a) 208(11) (2011) 2505-2510.

[48] T. Riberi-Béridot, M.G. Tsoutsouva, G. Regula, G. Reinhart, I. Périchaud, J. Baruchel, N. Mangelinck-Noël, Growth undercooling in multi-crystalline pure silicon and in silicon containing light impurities (C and O), Journal of Crystal Growth 466 (2017) 64-70.

[49] T. Riberi – Béridot, M.G. Tsoutsouva, G. Regula, G. Reinhart, F. Guittonneau, L. Barrallier, N. Mangelinck-Noël, Strain building and correlation with grain nucleation during silicon growth, Acta Materialia 177 (2019) 141-150.

[50] A. Tandjaoui, N. Mangelinck-Noël, G. Reinhart, B. Billia, X. Guichard, Twinning occurrence and grain competition in multicrystalline silicon during solidification, C.R. Physique 14 (2013) 8.

[51] T. Ervik, M. Kivambe, G. Stokkan, B. Ryningen, O. Lohne, Dislocation formation at Σ=27a boundries in multicrystalline silicon for solar cells, 26th European Photovoltaic Solar Energy Conference and Exhibition, Hamburg, Germany, 2011, pp. 1895-1899.

[52] T.N.T. Caliste, A. Drouin, D. Caliste, C. Detlefs, J. Baruchel, Rocking Curve Imaging Investigation of the Long-Range Distortion Field between Parallel Dislocations with Opposite Burgers Vectors, Applied Sciences 11(19) (2021) 9054.

[53] A. Derbouz, A. Slaoui, E. Jolivet, F. de Moro, C. Belouet, N-type silicon RST ribbon solar cells, Sol Energ Mat Sol C 107 (2012) 212-218.

[54] T.F. Ciszek, Techniques for the crystal growth of silicon ingots and ribbons, Journal of Crystal Growth 66(3) (1984) 655-672.

[55] A. Authier, Contrast of Dislocation Images in X-Ray Transmission Topography, Advances in X-ray Analysis 10 (1966) 9-31.

[56] J.A. Baker, T.N. Tucker, N.E. Moyer, R.C. Buschert, Effect of Carbon on the Lattice Parameter of Silicon, Journal of Applied Physics 39(9) (1968) 4365-4368.

[57] Y. Tao, T. Sorgenfrei, T. Jauß, A. Cröll, C. Reimann, J. Friedrich, J.J. Derby, Particle engulfment dynamics under oscillating crystal growth conditions, Journal of Crystal Growth 468 (2017) 24-27.

[58] M. Trempa, C. Reimann, J. Friedrich, G. Müller, A. Krause, L. Sylla, T. Richter, Defect formation induced by seed-joints during directional solidification of quasi-mono-crystalline silicon ingots, Journal of Crystal Growth 405(0) (2014) 131-141.

[59] N. Mangelinck-Noël, T. Duffar, Planar Front-Equiaxed Transition in semiconductor solidification: application to photovoltaic silicon, Transactions Indian Institute of Metals 60(2-3) (2007) 93-97.

[60] T. Duffar, Comprehensive review on grain and twin structures in bulk photovoltaic silicon, Recent Research Developments Crystal Growth 5 (2009) 61-111.

[61] A. Autruffe, V. Stenhjem Hagen, L. Arnberg, M. Di Sabatino, Dislocation generation at near-coincidence site lattice grain boundaries during silicon directional solidification, Journal of Crystal Growth 411 (2015) 12-18.

[62] B. Ryningen, G. Stokkan, M. Kivambe, T. Ervik, O. Lohne, Growth of dislocation clusters during directional solidification of multicrystalline silicon ingots, Acta Materialia 59(20) (2011) 7703-7710.

[63] M.G. Tsoutsouva, T. Riberi – Béridot, G. Regula, G. Reinhart, J. Baruchel, N. Mangelinck-Noël, In Situ Imaging of Dislocation Expansion in FZ-Si Seeds During Temperature Ramp Heating Process, Physica status solidi (a) A (2018) 1700758.

[64] W.M. Yim, R.J. Paff, Thermal expansion of AlN, sapphire, and silicon, Journal of Applied Physics 45(3) (1974) 1456-1457.

[65] J.R. O'Connor, Silicon Carbide, a High Temperature Semiconductor: Proceedings of the Conference on Silicon Carbide, Boston, Massachusetts, April 2-3, 1959, Pergamon Press1960.

[66] L.-C. Chuang, K. Maeda, H. Morito, K. Shiga, W. Miller, K. Fujiwara, In situ observation of interaction between grain boundaries during directional solidification of Si, Scripta Materialia 148 (2018) 37-41.

[67] K. Kutsukake, T. Abe, A. Usami, K. Fujiwara, I. Yonenaga, K. Morishita, K. Nakajima, Generation mechanism of dislocations and their clusters in multicrystalline silicon during two-dimensional growth, Journal of applied physics 110(8) (2011) 083530.

[68] J. Härtwig, Hierarchy of dynamical theories of x-ray diffraction for deformed and perfect crystals, Journal of Physics D: Applied Physics 34(10A) (2001) A70-A77.

[69] A. Authier, Étude de la distribution des déformations observables sur les topographies par rayonsX de cristaux presque parfaits, Journal de physique 27(1-2) (1966) 57-60.

[70] D.A. Hughes, N. Hansen, D.J. Bammann, Geometrically necessary boundaries, incidental dislocation boundaries and geometrically necessary dislocations, Scripta Materialia 48(2) (2003) 147-153.

[71] D. Kuhlmann-Wilsdorf, N. Hansen, Geometrically necessary, incidental and subgrain boundaries, Scripta Metallurgica et Materialia 25(7) (1991) 1557-1562.